

Direct Tensile Measurement for Cemented Paste Backfill

Andrew Pan *  and Murray Grabinsky 

Department of Civil and Mineral Engineering, University of Toronto, Toronto, ON M5S 1A4, Canada; murray.grabinsky@utoronto.ca

* Correspondence: andrew.pan@mail.utoronto.ca

Abstract: Tensile strength is a crucial parameter involved in the design and analysis of cemented paste backfill (CPB). The ability of CPB to withstand tensile forces is essential for the stability of the backfilled stopes, particularly in areas with high stress or deformation. The tensile strength is a critical design parameter used in sill mats to perform underhand cut-and-fill operations. This study presents a novel technique that utilizes rectangular dog-bone specimens and compression to tensile load converters to perform the direct determination of tensile strength. This study indicates that the prevailing assumption regarding the ratio of unconfined compressive strength (UCS) to tensile strength (i.e., 10:1 or 12:1) underestimates the strength. The results suggest a ratio closer to 3:1 or 4:1. The findings indicate that the ratio varies with the curing interval. Specifically, the tensile-to-compressive strength ratios were higher in early-age specimens, as tensile strength values do not increase at the same rate as those of compressive strength. This disparity has notable implications, as underestimating tensile strength via traditional UCS-to-tensile strength ratios could potentially inflate binder consumption. Our study underscores the importance of using direct tensile strength measurements to optimize mining operations.

Keywords: cemented paste backfill; direct tensile; dog-bone specimen; underhand cut-and-fill



Citation: Pan, A.; Grabinsky, M. Direct Tensile Measurement for Cemented Paste Backfill. *Minerals* **2023**, *13*, 1218. <https://doi.org/10.3390/min13091218>

Academic Editors: Haiqiang Jiang, Liang Cui, Nan Zhou, Xiwei Zhang, Abbas Taheri and Elsabe Kearsley

Received: 14 July 2023

Revised: 11 September 2023

Accepted: 14 September 2023

Published: 16 September 2023



Copyright: © 2023 by the authors. Licensee MDPI, Basel, Switzerland. This article is an open access article distributed under the terms and conditions of the Creative Commons Attribution (CC BY) license (<https://creativecommons.org/licenses/by/4.0/>).

1. Introduction

Cemented paste backfill (CPB) is a composite backfill technique used in hard rock mining as regional ground support and an aspect of mine waste management [1]. It has emerged as a cost-effective method of addressing mine tailings while providing ground support in underground operations [1,2]. Mine tailings are mixed with hydraulic binders, which are typically made of cement and slag, to create a homogenous mixture [3]. The mixture is placed into underground stopes and solidifies to create a stable and load-bearing mass, which aids in preventing ground subsidence and improving mine safety [4,5].

The strength and stability of CPB are crucial to its engineering applications [6,7]. The ability of CPB to withstand tensile forces is essential for the stability of the backfilled stopes, particularly in areas with high stress or deformation [8–10]. The tensile strength is a critical design parameter used in sill mats to perform underhand cut-and-fill operations [8,11,12]. Accurate tensile measurement is vital to optimize CPB mixtures and mitigate potential geo-hazards [13–15]. The direct tensile measurement of CPB has been a longstanding challenge [16]. The tensile strength of CPB is typically assumed based on unconfined compressive strength (UCS), having a ratio equal to UCS/10 or UCS/12 [1,7,11].

The challenges associated with the direct determination of tensile strength have been well documented in rock mechanics [10,17]. The fracture should occur in the central region of the specimen, i.e., away from the ends [17]. A small geometric imperfection or misalignment could introduce a bending moment, causing stress non-uniformity [17]. Various techniques have been developed to limit the stress concentrations and encourage the fracture in the central portion [14]. Dog-bone specimens and machined notches have been trialed [10]. Given their expensive and challenging nature, direct tensile tests are not routinely carried out [10,17]. These challenges are compounded by soft rocks and

geomaterials, as the geometrical tolerances, preparation methods, and smooth techniques are impractical [10,17].

Historically, the tensile strength of CPB has been determined using indirect methods, such as the Brazilian test, which correlates with the tensile strength by diametrically applying a compressive force to a cylindrical specimen [12,18]. While it has been widely used in research, it has limited industrial applications due to challenges associated with the soft and brittle responses of CPB [1,12,18]. As a result, researchers sought to develop direct tensile testing techniques through the dog-bone specimen [19], which involves directly applying the tensile force to the sample, thus providing a more accurate and reliable assessment of the tensile strength [20,21].

Despite the advancements in tensile strength measurements, there is limited work on CPB with tensile strengths greater than 1 MPa. Moreover, there are no detailed procedures and setups. Our study presents a direct tensile technique for CPB, including sample preparation and test apparatus. By utilizing improved dog-bone geometry, mold designs, a compression to tensile load converter, and stiffness analysis, we enhanced the testing setup to achieve more accurate results. This paper details these advancements and their applications.

2. Materials and Methods

2.1. Materials

The materials were sourced from the Macassa Mine, which is a high-grade gold mine located in Kirkland Lake, Ontario, Canada, approximately 500 km from Toronto. The mine employed long-hole stoping and underhand cut-and-fill methods [22,23]. The deposit consisted of a gold-bearing quartz vein, which was hosted within the Archean-age volcanic and Abitibi greenstone belt sedimentary rocks [24,25]. The ore body contained pyrite, chalcopyrite, sphalerite, and gold, as well as traces of sulfide minerals [23].

The CPB was composed of mine tailings, sand, and binder. Sand was added to enhance the grain size distribution and binder efficiency. The binder consisted of 10% cement and 90% slag. The mineralogy of the mine tailings and sand was analyzed via Rietveld Analysis using a Philips X'PERT Pro X-ray MRD diffractometer (Philips, Amsterdam, Netherlands) [26]. The specimens were ground with mortar and pestle to create a powder and oven dried at 40 °C. Next, 10% lithium fluoride was added into the samples as the baseline. The particle size distribution of mill tailing was determined via laser diffraction using a Beckman Coulter LS 13 320 at the Saskatchewan Research Council (SRC), Saskatoon, Canada. Table 1 shows the chemical composition of the binder from the Mill Report conducted by Lafarge Canada, and Tables 2 and 3 show the mineralogy of the mine tailing and sand, respectively. Figure 1 shows the Rietveld analysis of mineralogy, and Figure 2 shows the grain size distribution.

Table 1. Binder chemical composition.

Chemical Composition	CaO	SiO ₂	Al ₂ O ₃	MgO	SO ₃	Fe ₂ O ₃	Na ₂ O	K ₂ O
Portland cement, wt%	61.1	19.4	4.6	3.3	2.3	2	2	0.7
Blast furnace slag, wt%	37.1	36.1	10.4	13.2	3.4	0.7	0.4	0.5
Binder, wt%	39.5	34.5	9.8	12.3	3.3	0.8	0.6	0.5

Table 2. Mill tailing mineralogy.

Mineralogy	Volume, %
Microcline	40.00%
Dolomite	12.90%
Quartz	11.00%
Albite	5.30%
Clinocllore	3.20%
Pyrite	0.30%
Amorphous	27.20%

Table 3. Sand mineralogy.

Mineralogy	Volume, %
Quartz	41.20%
Microcline	40.80%
Albite	6.30%
Chlorite	2.60%
Muscovite	0.80%
Amorphous	8.40%

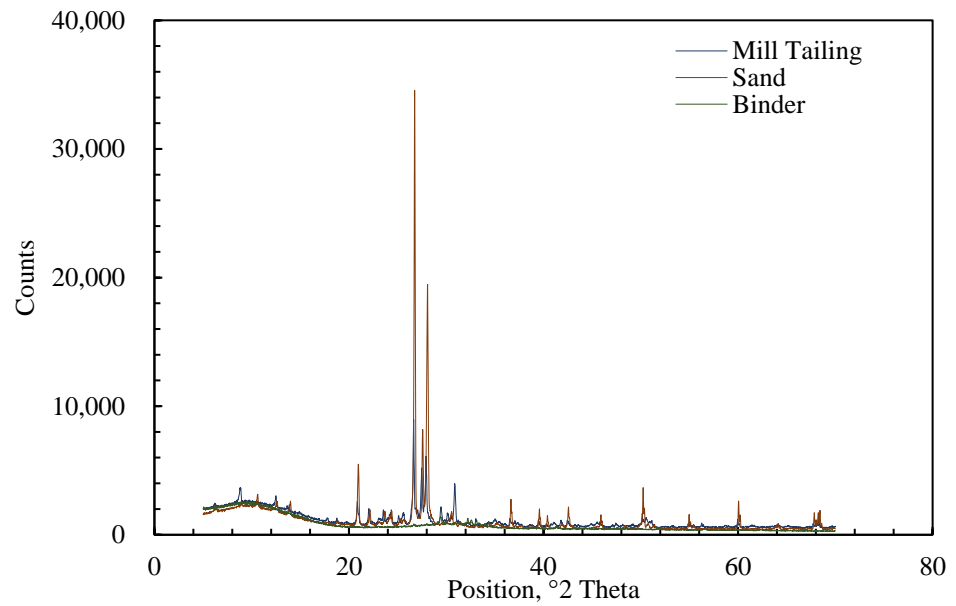


Figure 1. Rietveld analysis.

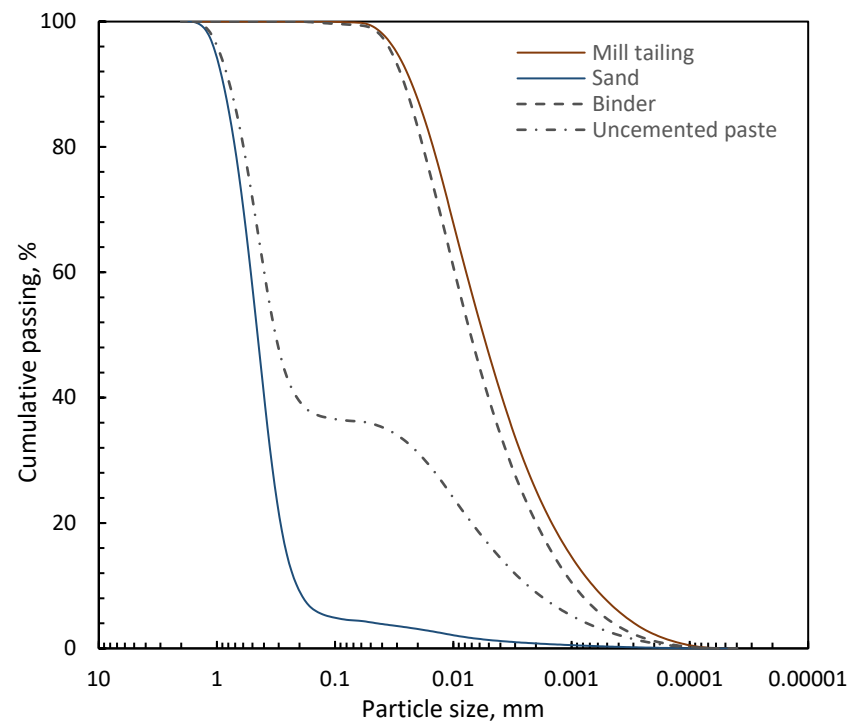


Figure 2. Grain size distribution.

The specimens were prepared based on mine practice with 10% binder content and a 2:1 ratio of sand to tailings based on the weights of solids with 28% water content by total weight. The constituents were mixed using an electric hand mixer for 10 minutes until a homogeneous paste with no segregation was formed [27]. The specimens were then cast in the sample enclosure. The samples were cured in water at 22 °C to preserve the sample's water content and simulate the saturated and high relative humidity conditions in the stope [14,28].

2.2. Test Apparatus

The test setup consisted of a four-part rectangular dog-bone mold (RDM) and a compression to tensile load converter (CTLC). The split mold was utilized to prepare the rectangular dog-bone specimen (RDS). The CTLC was used to convert the compression load to the tensile load.

2.2.1. Rectangular Dog-Bone Mold

The RDM was created to assess the RDS. The mold ensured that a uniform necking region was present in the sample. The mold was designed via AutoCAD 2024 V4.3, which is computer-aided design (CAD) software (San Francisco, CA, USA). The design file was exported as a stereolithography (SLT) file. The STL file was input into the Dremel DigiLab 3D Slicer V1.2.3 (Dremel, Breda, Netherlands), which transmitted the digital model into the printer instruction, G-code, as illustrated Figure 3.

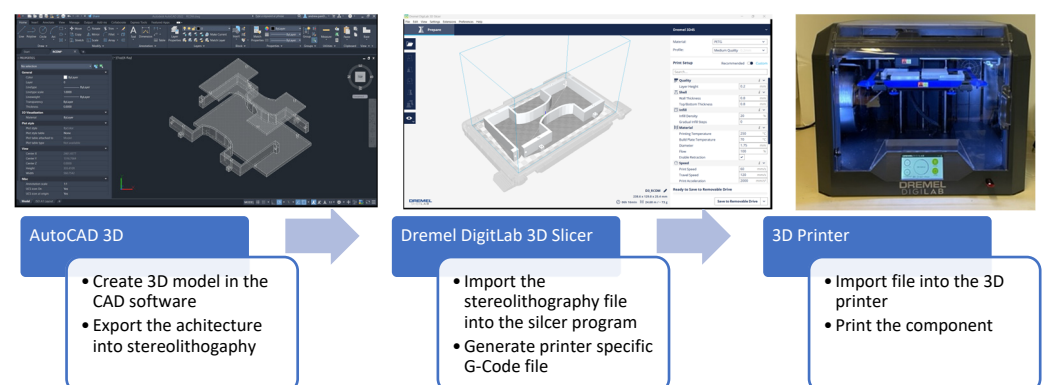


Figure 3. Additive manufacturing process schematic.

The molds were printed using Dremel 3D45, which is a fused deposition modeling (FDM) printer. The mold was printed with a PETG filament. The mold consisted of a base plate, two side enclosures, and a top cap, as shown in Figure 4. The mold was designed to minimize sample disturbance during demolding.

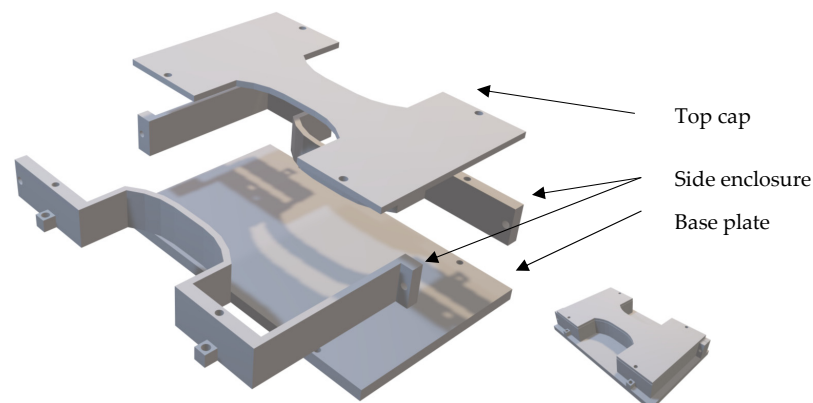


Figure 4. Rectangular dog-bone mold.

2.2.2. Compression to Tensile Load Converter

The apparatus comprised a load platform and a support platform, as shown in Figure 5. The load on the load platform was transmitted through the RDS to the support platform. The apparatus converted the compressive forces into the tensile load. The setup incorporated a self-aligning mechanism that limited bending moment and torsion and ensured a uniform and axial load on the CPB specimen [10,19–21].

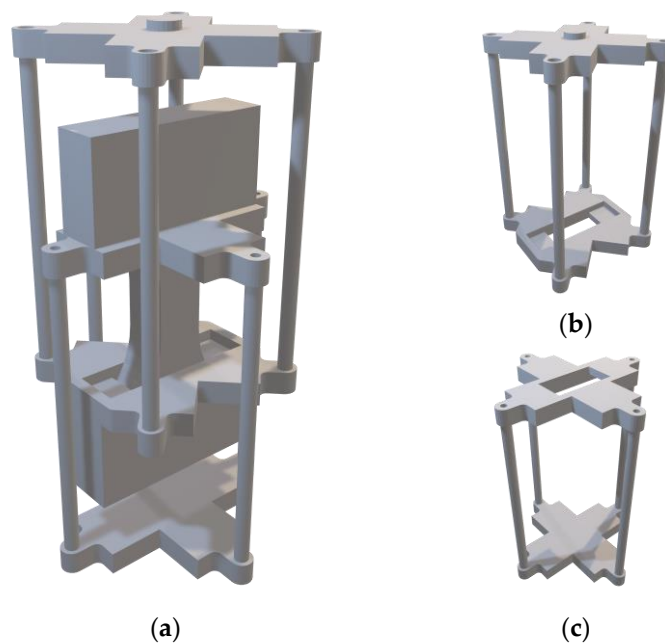


Figure 5. Compression to tensile load converter. (a) Assembly schematic. (b) Load platform schematic. (c) Support platform schematic.

The load platform consisted of the load plate, four rods, and two split load brackets. The support platform comprised the same setup with 2 split support brackets, as shown in Figure 6. The top and base brackets were made of aluminum to minimize the weight. The rods connecting the top and base brackets were made of stainless steel to enable stiffness and corrosion resistance. An alignment groove was cut into the bracket at a depth of 3.175 mm (1/8") to assist with the assembly process.



Figure 6. Compression to tensile load converter components.

2.3. Experimental Protocol

A test procedure was developed to enhance reliability and accuracy. This procedure encompassed sample preparation, sample extraction, and test strategy. A pouring technique

was developed to create a uniform section across the necking region. The sample extraction method and assembly procedure were developed to minimize sample disturbance.

2.3.1. Sample Preparation

CPB mixture was prepared by mixing the mine tailings, sand, binder, and process water until a homogeneous paste was formed. The material was cast into the mold. The CPB mixture was poured from the base up toward the necking region, as shown in Figure 7. The necking portion was continuously filled to avoid voids or defects.

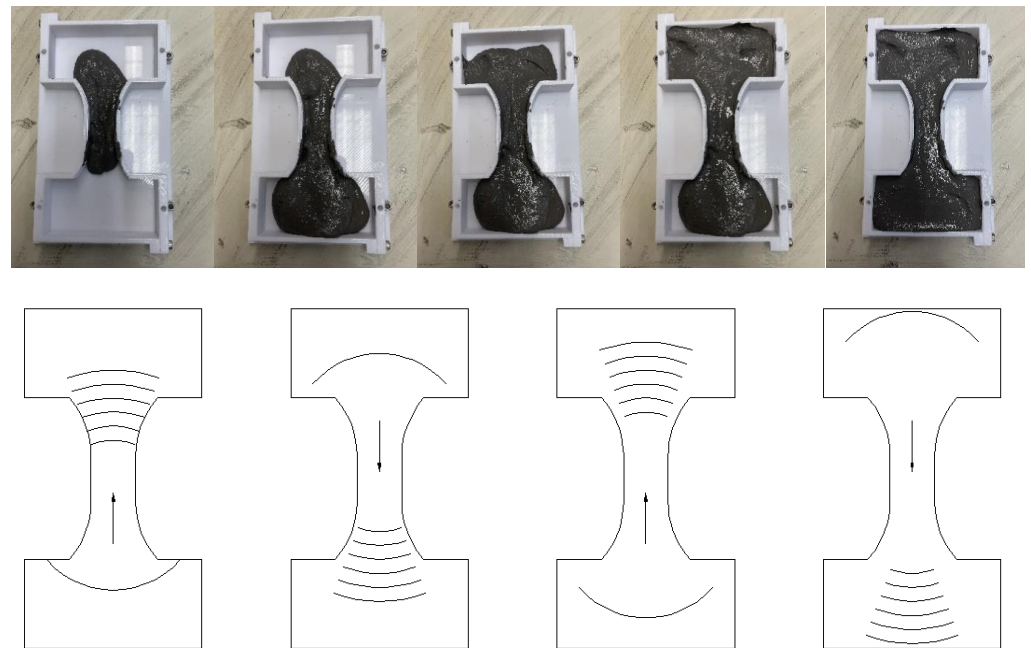


Figure 7. Filling strategy.

2.3.2. Demolding Process

An extraction method was developed to limit sample disturbance, as shown in Figure 8. The base plate was detached by applying even pressure around its perimeter. The top cap was removed via lifting at the side enclosures. The side enclosures were then removed from the specimen.



Figure 8. Demolding strategy.

2.3.3. Test Procedure

The assembly process consisted of three steps, as shown in Figure 9. The load split bracket was placed onto the specimen and fitted around the necking region. The bracket provided a connection between the specimen and the load converter, allowing the proper application of tensile forces. The support split bracket was positioned around the opposite end of the specimen and aligned with the load split bracket. The split bracket was then placed onto the load platform and attached to the support platform. Once secured, the load

platform with the specimen was flipped and positioned on top of the support platform. The test was conducted using a compression frame with Wille Geotechnic Tabletop Electromechanical Consolidation Apparatus, as shown in Figure 10. The specimen was loaded at 0.5 mm per minute.



Figure 9. Compression to tensile load converter assembly.



Figure 10. Test setup.

3. Results and Discussion

The tensile strength was calculated using the applied load, the weight of the load platform, and the specimen. This process is shown as follows [20]:

$$\sigma_t = \frac{P + W_l + W_s/2}{A} \quad (1)$$

where P is the applied load, W_l is the weight of the upper loading apparatus (the upper section of CTLC), W_s is the weight of the sample, and A is the area of necking. The direct tensile strength is analyzed using the UCS strength. The UCS tests were conducted in accordance with ASTM Standard D2166-06 Standard Test Method for the Unconfined Compressive Strength of Cohesive Soil [29]. Figure 11 shows the comparison between the direct tensile strength and the UCS strength. The results suggest that the current assumption of a tensile to UCS ratio of 1:10 or 1:12 underestimates the tensile strength. The data indicate that the ratio of compressive strength to tensile strength varies with the curing interval, ranging from one-fourth to one-third of the compressive strength. This

outcome can be attributed to the fact that the tensile strength does not increase at the same rate as compressive strength after the early ages.

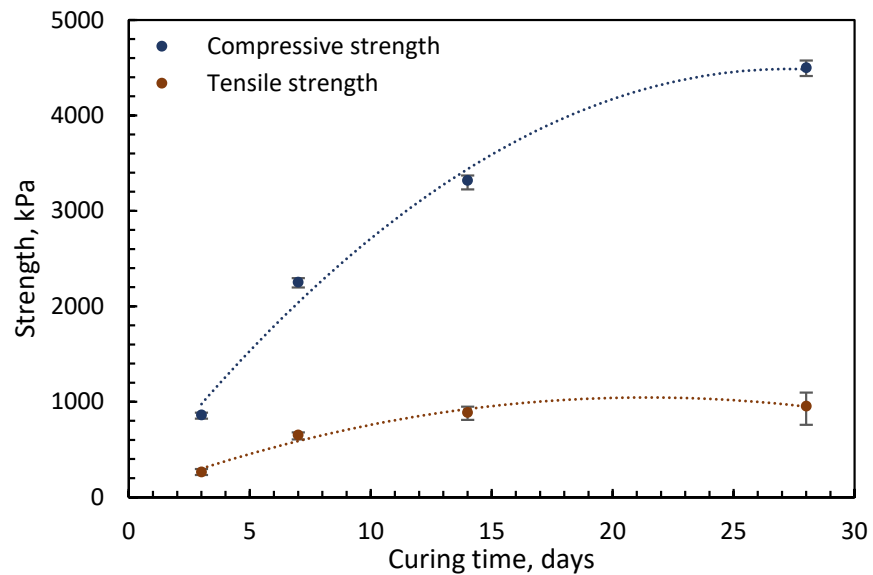


Figure 11. Comparison between tensile strength and UCS.

The stress displacements of the direct tensile of 10% CPB at 3-, 7-, 14-, and 28-day curing intervals are shown in Figure 12. The fracture is characterized by a linear elastic response to fracture, which is consistent with pure tensile failure [10]. The results show the first reported direct tensile strength at a 3-day curing interval and a tensile strength greater than one megapascal at a 28-day curing interval, which illustrates the effectiveness of the testing approach [30].

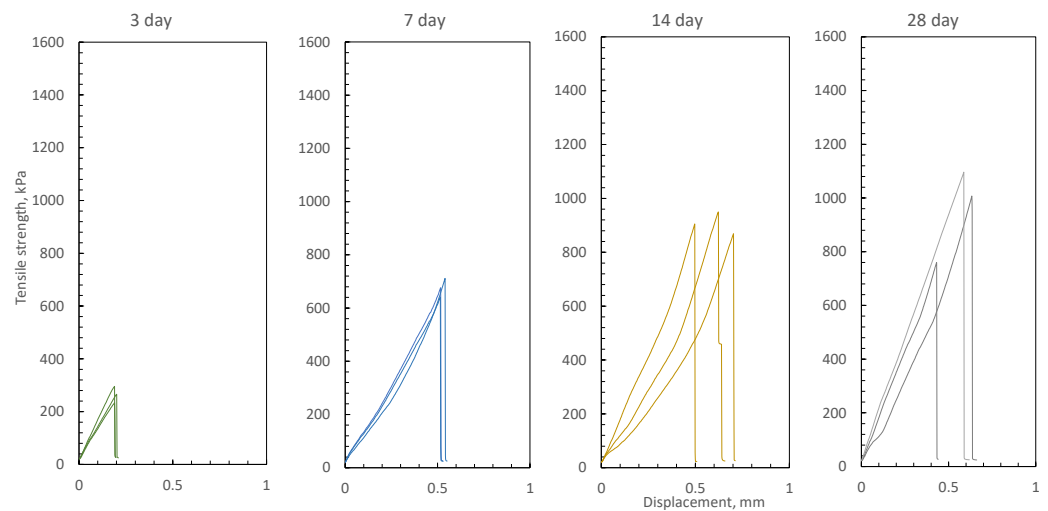


Figure 12. Stress displacement of the direct tensile test.

The fracture morphology is perpendicular to the direction of the tensile load, as shown in Figure 13. The fracture is consistent with the expected tensile failure at the necking of the specimen [10,17]. Even though the setup has enhanced the tensile mechanism, the bending moment is still present in the necking portion, as shown in Figure 13. To ensure statistical significance, the test should be conducted in a series of three.

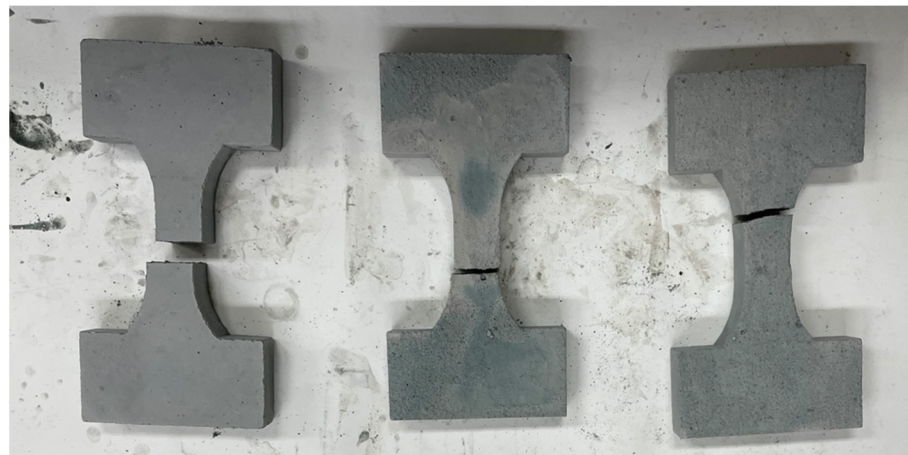


Figure 13. Fracture morphology.

The study reports the first direct tensile measurements found at a 3-day curing interval, and the first tensile strength is greater than one megapascal. These measurements are realized through two quantitative improvements, namely the optimized geometry of the dog-bone specimen and the stiffness analysis of the loading apparatus. These enhancements encompassed more accurate measurement techniques, refined the testing methods, improved material preparation, and advanced the testing apparatus.

3.1. Geometric Design

The dog-bone geometry was refined to limit the bending moment from the lateral load, increase the shear resistance in the flange, and distribute the load across the contact surface. This outcome is achieved by decreasing the necking length from 50.8 mm to 25.4 mm, increasing the flange depth and width by 6.4 mm, as shown in Figure 14.

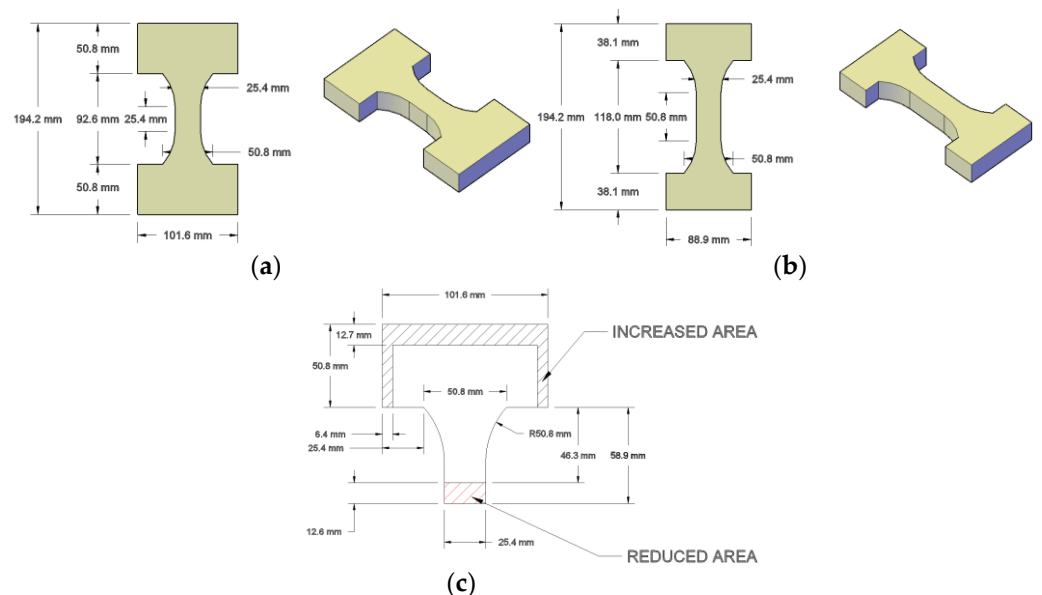


Figure 14. Geometric comparison. (a) Revised specimen. (b) Original geometry. (c) Geometric comparison.

The revised geometry of the dog-bone specimen reduced the bending moment from lateral forces by 42.8% [20]. The decrease in the bending stress contributes to a more

uniform stress distribution through the specimen and minimizes the potential of premature failure resulting from bending.

$$M = 2 \times M_{\text{mid}} = 2 \times PL \tag{2}$$

$$M_{\text{comp}} = \frac{L_1P - L_2P}{L_1P} \times 100\% = 2 \times \frac{58.9 - 46.3}{58.9} \times 100\% = 42.8\% \tag{3}$$

The revised dog-bone geometry also increased the shear resistance in the flange. The block shear resistance increased by 66.7%, which enabled the specimen to withstand higher tensile forces.

$$S = F_{\text{ult}}A = F_{\text{ult}}tw \tag{4}$$

$$S_{\text{comp}} = \frac{2F_{\text{ult}}h_2w - 2F_{\text{ult}}h_1w}{2F_{\text{ult}}h_1w} \times 100\% = \frac{2h_2 - 2h_1}{2h_1} \times 100\% = 66.7\% \tag{5}$$

By optimizing the flange shape and dimensions, the load was more uniformly distributed across the contact surface, which reduced stress concentrations and the risk of premature failure. This outcome contributes to more accurate and reliable strength measurements.

$$I_w = wt \tag{6}$$

$$I_{w\text{-comp}} = \frac{2w_2t - 2w_1t}{2w_1t} \times 100\% = \frac{2 \times 25.4 - 2 \times 19.05}{2 \times 19.05} \times 100\% = 66.7\% \tag{7}$$

Figure 15 shows the geometry of the dog-bone specimen. The geometric drawings, stereolithography (STL), and drawing exchange format (DXF) of the CTLC and RCDM are included in the supplementary file.

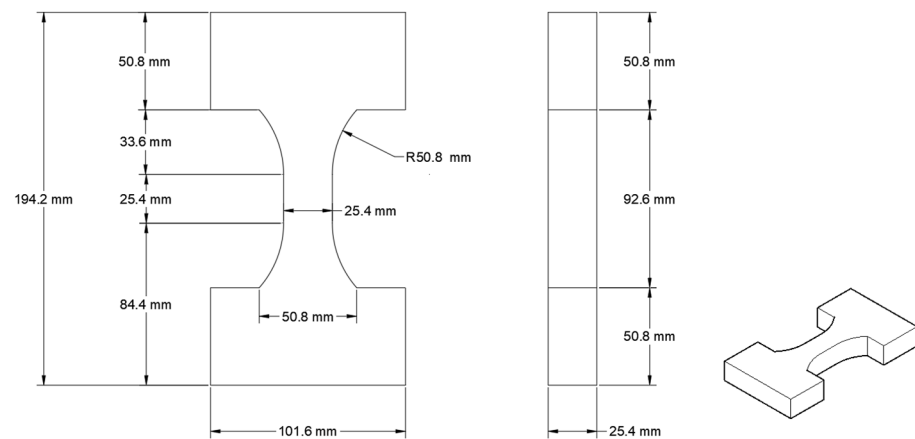


Figure 15. Dog-bone geometry.

3.2. Stiffness Analysis

A stiffness analysis was developed to ensure the strength and stiffness of the loading apparatus. Euler’s buckling theorem was employed to examine the metal rod’s buckling potential, and the shear theorem was used to assess the bracket’s shear resistance.

3.2.1. Critical Buckling Analysis for Rods

The rods are considered to be slender members. Euler's buckling theorem was used to determine the critical buckling load required to ensure rod stability under compressive loads [31,32].

$$\text{Critical buckling load} = \frac{\pi^2EI}{L^2} = \frac{\pi^3ED^4}{64L^2} \tag{8}$$

where L is the length of rod, E is the modulus elasticity, I is the moment of inertia, and D is the diameter of the rod. The critical load for the load platform can be determined as follows:

$$P = \varphi \frac{\pi^3 ED^4}{64L^2} \times 4 \text{ rod} = 0.6 \frac{\pi^3 ED^4}{16L^2} \quad (9)$$

where P is critical compressive load, and φ is the resistance factor (set at 0.6).

3.2.2. Shear Analysis

The shear theorem was used to calculate the maximum shear force experienced by the bracket during tensile testing. This theorem is shown as follows [31]:

$$S = \varphi F_{\text{ult}} A = 0.6 F_{\text{ult}} A \quad (10)$$

where S is the critical shear load, φ is the resistance factor (set at 0.6), F is the shear strength of material used to construct the bracket, and A is the minimal cross-sectional area of the bracket.

4. Conclusions

Accurate tensile strength measurement is crucial for the design and analysis of sill mats in underhand cut-and-fill operations and ensuring mine safety. This paper presented a mechanically rigorous method for the direct determination of CPB tensile strength. The test setup incorporates a rectangular dog-bone specimen and compression to tensile load converter with a self-aligning mechanism. The results indicate that the current assumption of tensile strength being 1:10 or 1:12 of UCS underestimates the tensile strength. The results show a ratio of 1:3 or 1:4 of UCS to tensile strength.

The results indicate that the ratio of tensile to compressive strength is not a constant value. Specifically, early-age tensile strengths display strength ratios that are higher than those observed in more mature specimens. This result can be attributed to the fact that tensile strength values do not increase at the same rate as compressive strength values after early ages. These findings highlight the need for revised guidelines, particularly to emphasize the importance of conducting tensile strength tests at different stages of material maturity to achieve a more accurate assessment. This disparity has notable implications for the design of and costs associated with CPB, specifically the binder content estimation for strength. Underestimating tensile strength via traditional UCS-to-tensile strength ratios potentially inflates binder consumption, resulting in unnecessary financial burdens. By adopting direct tensile testing, mine operators could significantly reduce their operating costs. This technique offers valuable insights into the mechanical properties of CPBs and has the potential to contribute to more efficient and sustainable mining practices. It has already been adopted by two mining companies and the backfilling consultancy firm Paterson and Cooke.

The tensile strength values represent intrinsic material properties and do not account for cold joints, shrinkage cracks, or micro-fractures that may occur in real-world applications. Further research is needed to better understand the effects of cold joints, shrinkage cracks, and micro-fractures on CPB performance.

Supplementary Materials: The supporting information can be accessed via the following link: <https://www.mdpi.com/article/10.3390/min13091218/s1>. The supplementary files include the drawing exchange format (DXF) and stereolithography (STL) files used in the rectangular dog-bone mold (RDM) and the DXF file used in the compression to tensile load converter (CTL). We encourage mine operators and researchers to utilize our design to further their work. However, we do not provide a warranty for the design and cannot be held liable for any misuse or errors within the files.

Author Contributions: Conceptualization, A.P. and M.G.; methodology, A.P.; software, A.P.; validation, A.P. and M.G.; formal analysis, A.P.; investigation, A.P.; resources, M.G.; data curation, A.P.; writing—original draft preparation, A.P.; writing—review and editing, A.P. and M.G.; visualization, A.P.; supervision, M.G.; project administration, A.P.; funding acquisition, A.P. and M.G. All authors have read and agreed to the published version of the manuscript.

Funding: This project is supported by the Mitacs Accelerate Program, the Queen Elizabeth II Science and Technology Program (QEII-GSST), and an industrial funding and partnership with Agnico Eagle Mines.

Data Availability Statement: All data, models, and code that support the findings of this study are available from the corresponding author upon reasonable request.

Acknowledgments: We would like to thank Agnico Eagle Mines for their provision of materials and insights related to mining practices. We also thank Autodesk for providing AutoCAD through the Autodesk Education Community. We would also like to thank Olga Perebatova for her expert assistance during the X-ray diffraction (XRD) analysis and interpretation stages.

Conflicts of Interest: The authors declare no conflict of interest.

References

1. Paterson & Cooke. *Mine Backfill Design & Operation Course*; Paterson & Cooke: Sudbury, ON, Canada, 2019.
2. Yilmaz, E.; Cao, S.; Wu, D. Advances in the Design and Implementation of Cementitious Backfills. *Front. Mater.* **2022**, *9*, 964111. [[CrossRef](#)]
3. Yang, L.; Li, J.; Liu, H.; Jiao, H.; Yin, S.; Chen, X.; Yu, Y. Systematic review of mixing technology for recycling waste tailings as cemented paste backfill in mines in China. *Int. J. Miner. Metall. Mater.* **2023**, *30*, 1430. [[CrossRef](#)]
4. Yilmaz, E.; Belem, T.; Benzaazoua, M. Effects of curing and stress conditions on hydromechanical, geotechnical and geochemical properties of cemented paste backfill. *Eng. Geol.* **2014**, *168*, 23–37. [[CrossRef](#)]
5. Skrzypkowski, K. The Influence of Room and Pillar Method Geometry on the Deposit Utilization Rate and Rock Bolt Load. *Energies* **2019**, *12*, 4770. [[CrossRef](#)]
6. Pakalnis, R.; Caceres, C.; Clapp, K.; Morin, M.; Brady, T.; Williams, T.; Blake, W.; MacLaughlin, M. Design Spans—Underhand Cut and Fill Mining. In Proceedings of the 107th Canadian Institute of Mining Annual General Meeting, Toronto, ON, Canada, 1–9 April 2005; pp. 1–9.
7. Keita, A.M.T.; Jahanbakhshzadeh, A.; Li, L. Numerical analysis of the failure mechanisms of sill mats made of cemented backfill. *Int. J. Geotech. Eng.* **2021**, *16*, 802–814. [[CrossRef](#)]
8. Keita, A.M.T.; Jahanbakhshzadeh, A.; Li, L. Numerical analysis of the stability of arched sill mats made of cemented backfill. *Int. J. Rock Mech. Min. Sci.* **2021**, *140*, 104667. [[CrossRef](#)]
9. Raffaldi, M.J.; Seymour, J.B.; Richardson, J.; Zahl, E.; Board, M. Cemented Paste Backfill Geomechanics at a Narrow-Vein Underhand Cut-and-Fill Mine. *Rock Mech. Rock Eng.* **2019**, *52*, 4925–4940. [[CrossRef](#)]
10. Perras, M.A.; Diederichs, M.S. A Review of the Tensile Strength of Rock: Concepts and Testings. *Geotech. Geol. Eng.* **2014**, *32*, 525–546. [[CrossRef](#)]
11. Mitchell, R.J. Sill mat evaluation using centrifuge models. *Min. Sci. Technol.* **1991**, *13*, 301–313. [[CrossRef](#)]
12. Johnson, J.C.; Seymour, J.B.; Martin, L.A.; Stepan, M.; Arkoosh, A.; Emery, T. Strength and Elastic Properties of Paste Backfill at the Lucky Friday Mine, Mullan, Idaho. In Proceedings of the U.S. Rock Mechanics/Geomechanics Symposium, San Francisco, CA, USA, 29 June–1 July 2015.
13. Grabinsky, M.; Bawden, W.; Thompson, B. Required Plug Strength for Continuously Poured Cemented Paste Backfill in Longhole Stopes. *Mining* **2021**, *1*, 80–99. [[CrossRef](#)]
14. Thompson, B.D.; Bawden, W.F.; Grabinsky, M.W. In-Situ Backfill Monitoring—Lessons Learned and a New Case Study. *Can. Geotech. J.* **2012**, *49*, 755–772. [[CrossRef](#)]
15. Kuzmenko, O.; Dychkovskiy, R.; Petlovanyi, M.; Buketov, V.; Howaniec, N.; Smoliński, A. Mechanism of Interaction of Backfill Mixtures with Natural Rock Fractures within the Zone of Their Intense Manifestation while Developing Steep Ore Deposits. *Sustainability* **2023**, *15*, 4889. [[CrossRef](#)]
16. Grabinsky, M.; Jafari, M.; Pan, A. Cemented Paste Backfill (CPB) Material Properties for Undercut Analysis. *Mining* **2022**, *2*, 103–122. [[CrossRef](#)]
17. Coviello, A.; Lagioia, R.; Nova, R. On the measurement of the tensile strength of soft rocks. *Rock Mech. Rock Eng.* **2005**, *38*, 251–273. [[CrossRef](#)]
18. Komurlu, E.; Kesimal, A.; Demir, S. Experimental and numerical analyses on determination of indirect (splitting) tensile strength of cemented paste backfill materials under different loading apparatus. *Geomech. Eng.* **2016**, *10*, 775–791. [[CrossRef](#)]
19. Fuenkajorn, K.; Klanphumeesri, S. Laboratory Determination of Direct Tensile Strength and Deformability of Intact Rocks. *Geotech. Test. J.* **2011**, *34*, 97–102.
20. Pan, A.; Grabinsky, M. Tensile Strength of Cemented Paste Backfill. *Geotech. Test. J.* **2021**, *44*, 1886–1897. [[CrossRef](#)]

21. Guo, L.; Peng, X.; Zhao, Y.; Liu, G.; Pan, A. Experimental Study on Direct Tensile Properties of Cemented Paste Backfill. *Front. Mater.* **2022**, *2022*, 864264. [[CrossRef](#)]
22. Agnico Eagle. Macassa. Available online: <https://www.agnicoeagle.com/English/operations/operations/Macassa-Mine/default.aspx> (accessed on 7 April 2023).
23. Mining Data Solution. Macassa Mine. Available online: <https://miningdataonline.com/property/453/Macassa-Complex.aspx> (accessed on 7 April 2023).
24. Kerrich, R.; Watson, G.P. The Macassa Mine Archean lode gold deposit, Kirkland Lake, Ontario; geology, patterns of alteration, and hydrothermal regimes. *Econ. Geol.* **1984**, *79*, 1104–1130. [[CrossRef](#)]
25. Stammers, L.K. Geochemical Constraints of the Gold Mineralization Sources from the South Mine Complex and the Main/'04 Breaks, Macassa Mine, Kirkland Lake, Ontario. Master's Thesis, Western University, London, ON, Canada, 2016.
26. Rietveld, H.M. A profile refinement method for nuclear and magnetic structures. *J. Appl. Crystallogr.* **1969**, *2*, 65–74. [[CrossRef](#)]
27. Jafari, M.; Shahsavari, M.; Grabinsky, M. Cemented Paste Backfill Laboratory study: Sample preparation challenges. In Proceedings of the 70th Canadian Geotechnical Conference, Ottawa, ON, Canada, 23–26 September 2018.
28. Pan, A.; Grabinsky, M. Mechanical Characterization of Cemented Paste Backfill. *Eng* **2023**, *1*, 738–747. [[CrossRef](#)]
29. ASTM, *ASTM D2166–06*; Standard Test Method for Unconfined Compressive Strength of Cohesive Soil. ASTM International: West Conshohocken, PA, USA, 2006.
30. Hu, Y.; Hang, B.; Zhang, B.; Li, K. Force Analysis and Strength Determination of the Cemented Paste Backfill Roof in Underhand Drift Cut-and-Fill Stopping. *Appl. Sci.* **2023**, *13*, 855. [[CrossRef](#)]
31. Beer, F.P.; Johnston, R.E.; De Wolf, J.T.; Mazurek, D.F. *Mechanics of Materials*, 6th ed.; McGraw-Hill Science: New York, NY, USA, 2011.
32. Euler, L. *Methodus Inveniendi Lineas Curvas Maximi Minimive Proprietate Gaudentes Sive Solutio Problematis Isoperimetrici Latissimo Sensu Accepti*; Marc-Michel Bousquet: Geneva, Switzerland, 1744.

Disclaimer/Publisher's Note: The statements, opinions and data contained in all publications are solely those of the individual author(s) and contributor(s) and not of MDPI and/or the editor(s). MDPI and/or the editor(s) disclaim responsibility for any injury to people or property resulting from any ideas, methods, instructions or products referred to in the content.